Development of a Low-cost, Sensitivity-optimized Fluorescence Sensor for Visible Spectrum Analysis

Zekun Wu, Scott E. Crawford, Michael Buric, Zach Splain, and Kevin P. Chen

Abstract: This paper presents an economically viable, sensitivity-optimized fluorescence sensor for detecting low concentrations of fluorophores in the visible spectrum range. The sensor employs a deep ultraviolet (DUV) 275-nm LED and a dichroic mirror to establish a co-axial optical path for excitation and emission. Instead of utilizing a general-purposed spectrometer optimized for high spectral resolution, the sensor strikes a balance between resolution and sensitivity by using an appropriate aperture size and optimized optical design tailored for the spectral characteristics of fluorophores. The manuscript demonstrates measurements of ppb-level rare earth element (REE) samples containing terbium (Tb), europium (Eu), dysprosium (Dy), and samarium (Sm) in aqueous solutions. Through balanced design that optimizes collection of fluorescence emission without losing spectral information, this work shows the feasibility of developing a low-cost, compact, and highly sensitive fluorescence sensors with improved detection sensitivity when compared to bench-top commercial spectrofluorometers at far higher costs.

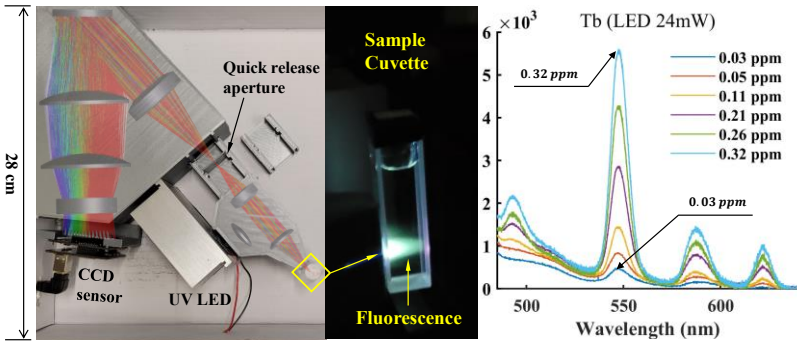

Keywords: sensitivity-optimized, low-cost, fluorescence sensor, spectrofluorometer, rare-earth elements (REEs)

I. Introduction

Fluorescence sensor, a device utilized for evaluating photoluminescence-related properties such as fluorescence emission intensity, spectrum, and polarization [1], is one of the most widely used optical sensing techniques applied across a broad range of applications, including but not limited to chemical and biological sensing [2-7], environment monitoring [8-13], material characterization [14-17], and probing energy transfer processes [18-20].

In general, a fluorescence sensor utilizes short-wavelength light sources to optically excite fluorophores. High-pressure xenon (Xe) arc lamps are one of the most versatile light sources for a steady state spectrofluorometer [1]. However, light-emitting diodes (LEDs) are increasingly popular in fluorescence spectroscopy due to their advantages, such as compactness, lower power consumption, cost-effectiveness, and lower infrared and heat emission [1,21]. Scientific communities and industries have developed many variants of compact fluorescence sensors with LEDs as excitation source [3,8-12,17]. Most LED-based fluorescence sensors utilize a spectrometer to decompose optical emissions into constituent spectra, then use a general-purpose CCD or CMOS imaging sensors to detect spectral signals. The optical design of a general-purpose spectrometer typically focuses on optimizing diffraction-limited resolution for a given aperture or slit width on the order of micrometers.

However, for most fluorophores that are commonly studied, the tight spacing of vibrational energy levels produces a wide range of emission photon energies (wavelengths), resulting in broad-band spectral features [1]. Thus, while high spectral resolution can be excessive for most broad-band fluorescence applications, it may impose inherent limitations on the sensitivity because of poor optical signal collection efficiency due to the use of a narrow aperture or slit. To detect extremely weak optical emissions using spectrometers with low collection efficiency, expensive and highly sensitive imaging sensors such as cryogenically cooled back-thinned CCD sensors or intensified CCD (ICCD) sensors are needed. This significantly increases the cost of high-performance fluorescence sensors and limits their applicability outside well-maintained laboratories. Resolution-optimized spectrometers can pose an even greater challenge for LED-based fluorescence sensors, as

This work was supported by the National Energy Technology Laboratory's ongoing research under the Research Support Services (RSS) contract [89243318CFE000003]. (Corresponding author: Kevin P. Chen.)

Zekun Wu, Scott E. Crawford and Michael Buric are with the National Energy Technology Laboratory, 3610 Collins Ferry Road, Morgantown, WV 26505, USA. (e-mail: zew19@pitt.edu; scott.crawford@netl.doe.gov; michael.buric@netl.doe.gov).

Zekun Wu, Zach Splain and Kevin P. Chen are with the Department of Electrical and Computer Engineering, Swanson School of Engineering, University of Pittsburgh, Pittsburgh, PA 15260, USA (e-mail: zew19@pitt.edu; zsplain@gmail.com; pchenc@gmail.com).

Scott E. Crawford is also with NETL Support Contractor, 626 Cochrans Mill Rd., Pittsburgh, Pennsylvania 15236, USA (e-mail: scott.crawford@netl.doe.gov).

they typically operate with relatively low excitation power to maintain low cost and compactness.

This paper presents an alternative approach to improve sensitivity for fluorescence sensors by designing a sensitivity-optimized but resolution-appropriated fluorescence sensor. Through an optical design that prioritizes fluorescence signal collection efficiency, this paper demonstrates a fluorescence sensor capable of detecting ppb-levels of economically critical rare earth element (REE) samples of terbium (Tb), europium (Eu), dysprosium (Dy), and samarium (Sm) in aqueous solutions. The performance of the low-cost fluorescence sensor is compared to that of a research-grade desktop commercial spectrofluorometer at far higher costs.

II. Mathematical Model

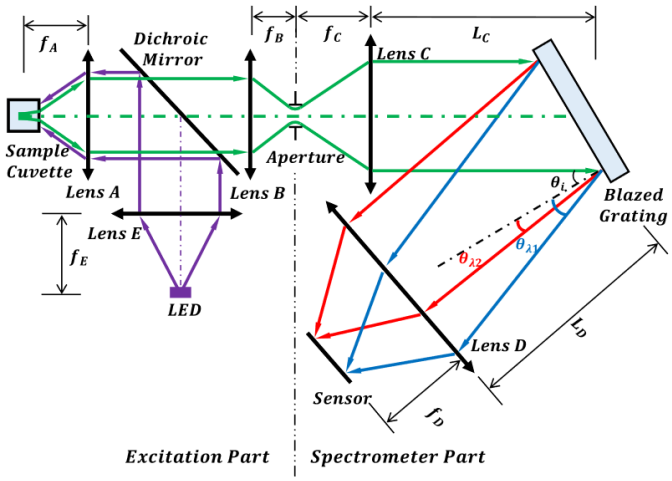

Fig. 1. Simplified model of the fluorescence sensor.

A. Co-axial Configuration

The excitation part of the fluorescence sensor consists of a deep ultraviolet (DUV) light emitting diode (LED), a dichroic mirror, and three collimating lenses A, B, and E as shown in Fig. 1. The excitation light from the 275 nm LED (XST-3535-UV, Luminus Inc.) is collimated by lens E and then reflected by a single-edge dichroic mirror (Semrock FF347-Di01, 25 mm × 36 mm) employed at 45° to the central axis. The excitation light is then focused into a sample cuvette, where the fluorescence is emitted. A portion of the fluorescence returns through lens A, passes straight through the dichroic mirror, and is then focused by lens B through the aperture.

The dichroic mirror, which separates the UV excitation and visible-wave fluorescence emission, exhibits at least 97% reflection for 240-325 nm at 45° and at least 93% transmission for 380-800 nm [22]. The focusing of excitation and backscattering of fluorescence shares the same optical axis, so there is no need to align the emission axis with the excitation axis at the focal point. This co-axial arrangement of excitation and emission light maximizes the collection of fluorescence and enables quick, alignment-free tests of multiple samples. The wavelength-dependent transmission of the dichroic mirror also minimizes pump-wave backscattering toward the detector.

B. Nonlinear Programming

Grating is the crucial component of the lens-grating-lens (LGL) spectrometer. To maximize the grating efficiency at specific diffraction order, a blazed reflective grating, also known as an echelette grating, is the preferred option. A blazed grating is designed to maximize grating efficiency in a specific diffraction order, generally the first order, while operating at a specific wavelength, known as the blaze wavelength [23]. As shown in the spectrometer part of Fig. 1, θ_i indicates the wavefront incident angle, and $\theta_{\lambda 1}$, $\theta_{\lambda 2}$ denote the diffracted angles for the minimum and maximum design wavelengths in the first diffraction order, respectively. The diffracted angle θ can be obtained from the following grating equation [23]:

$$\theta(\lambda, \theta_i) = \sin^{-1}(Gm\lambda - \sin\theta_i) \tag{1}$$

where G represents the groove frequency or groove density, usually measured in grooves per millimeter, while m indicates the diffraction order. The value of m is equal to 1 for maximum efficiency for a blazed grating.

The envisaged bandwidth spans from 450 nm to 750 nm, and the expected spectral resolution on the sensor plane is approximately 7 nm per millimeter. The spectrum resolution can be characterized by the reciprocal linear dispersion P, which can be obtained by the following equation [23]:

$$P = Gmf_D \cdot sec[\theta(\lambda, \theta_i)] \tag{2}$$

where f_D refers to the effective focal length of the post-grating lens system, which is simplified and denoted as lens D in Fig. 1, and θ is the diffracted angle for a given wavelength λ and incident angle θ_i.

This optical system can be considered as an imaging system that images the fluorescence spot from the cuvette to the sensor plane. An essential design parameter is the system magnification, which equals the ratio of the image distance to the object distance in a finite conjugate system. There are 3 conjugate planes in the system: the fluorescence plane in the sample cuvette, the aperture plane located between lens B and C, and the sensor plane, as depicted in Fig. 1, leading to the following equation:

$$\beta = \frac{f_B}{f_A} \cdot \frac{f_D}{f_C} = \frac{f_D}{f_A} \cdot \frac{D_B}{D_C} \tag{3}$$

where β represents the system magnification, while D_B and D_C denote the clear apertures for lens B and C, respectively, typically exceeding 90% of their diameter. Hence, we have formulated a nonlinear programming objective function that can be expressed as the equation below:

$$\min_{G,\theta_i,f_{A,D},D_{B,C}} \sum_{\lambda} [W_\lambda \cdot (P - P_0)^2] + [ReLU(\beta - \beta_0)]^2 \tag{4}$$

where W_λ denotes a normalized gaussian window for optimal performance centered at the central wavelength of 600 nm. P_0 and β_0 represent the design, set at 7 nm per millimeter and 1, respectively. A smaller system magnification results in higher spectral resolution, thus a system magnification less than β_0 is considered acceptable. Therefore, a rectified linear activation unit (ReLU) is employed to incorporate penalties only when β surpasses β_0.

Given the limited options of commercial off-the-shelf optics and necessary spacing between components, nonlinear programming can be constrained. For instance, typical

commercial gratings are available in sizes of 12.7 mm, 25.4 mm, or 50.8 mm, and offer groove density ranging from 300 to 1800 grooves per millimeter. Given these constraints, MATLAB nonlinear programming solver *fmincon* with interior-point algorithm was implemented [24], resulting in an optimized groove-density value of 1220.5 grooves/mm. Nevertheless, since the nearest commercial option was 1200 grooves/mm, we set this as the fixed value and proceeded with the subsequent optimization. Following several iterations, we successfully obtained commercially available values for θ_i, f_A, f_D, D_B and D_C, measuring 46.1°, 40.1 mm, 118.5 mm, 23 mm, and 45 mm respectively. Given focal length and clear aperture of a lens, the numerical aperture (NA) can be easily obtained by the following equation [25]:

$$NA = n \cdot sin\left[tan^{-1}\left(\frac{D_A}{2f_A}\right)\right] \quad (5)$$

where n is the index of refraction of the medium in which the lens operates (n is equal to 1 in our case), and D_A and f_A are the clear aperture and focal length of lens A, respectively. Given that lens A plays a dual role in excitation focusing and fluorescence collection, the numerical aperture (NA) of lens A determines the maximum possible NA of the system. Thus, lenses with NAs of approximately 0.3 were deliberately selected for lenses A, B, and C. Further details regarding NA of lens E will be expounded upon in Section III A.

III. ZEMAX Simulation and Optimization

A. LED Collimation and Fluorescence Profile

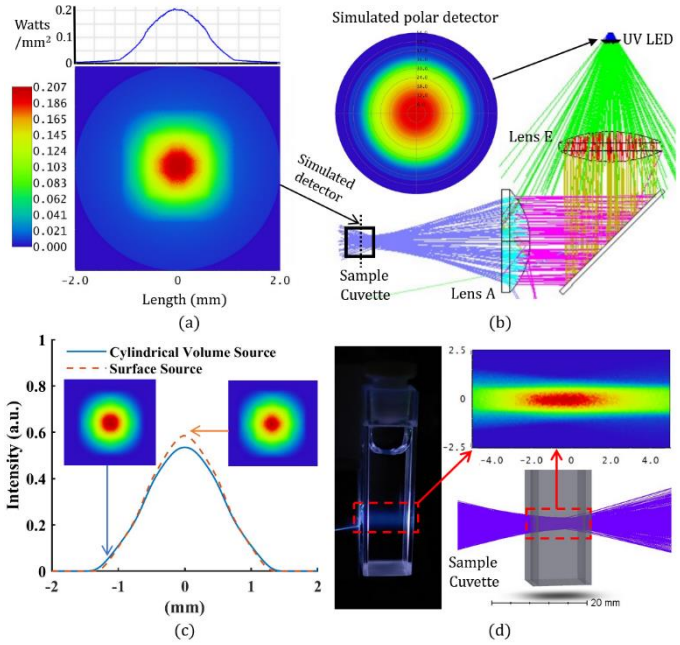

Fig. 2. (a) Simulated image of the LED square emitting pattern inside the cuvette where liquid samples are excited. (b) Simulated angular radiation pattern and collimation of the LED. (c) Simulated image intensity profiles of volume and surface source. (d) LED focal point inside sample (distilled water) cuvette and simulated intensity profile near the focal point inside cuvette (CV10Q35F, Thorlabs Inc.).

The excitation light source utilized is a 275 nm UV LED (XST-3535-UV, Luminus Inc.). The emission angle of LED is roughly ±40° (NA 0.65) and its angular radiation pattern is modeled in ZEMAX based on the datasheet [26]. To validate the simulated radiation pattern, a polar detector is situated in front of the UV LED as depicted in Fig. 2b, with 70.4% of total power contained within ±21.1° (NA 0.36)

Fig. 2b also delineates the collimation of the LED achieved by lenses E (NA 0.36) and A (NA 0.3). While using a relatively low NA lens (NA 0.3) for collimation is reasonable, it is not as high as in systems utilizing expensive high-NA condenser lenses, which also exhibit extremely short focal lengths. Notably, since lens A and E constitute an imaging system, a short focal length for lens E would result in significant magnification on the focal plane (inside the cuvette) of lens A pursuant to (3) outlined in section II, thereby lowering the energy density and fluorescence concentration. Thus, it is preferable for lens E to have a NA slightly greater than the system NA (0.3) to collimate more power from the light source while maintaining moderate magnification. Consequently, we selected an ultraviolet fused silica (UVFS) bi-convex lens with an NA of 0.36 as lens E.

The simulated projected square emitting pattern of the LED collected by a 4x4 mm square detector inside the cuvette is shown in Fig. 2a, where more than 90% of the energy is concentrated within a 2x2 mm square area. Because the fluorescence area is a three-dimensional space, we simulated both 3D cylindrical volume source (based on profiles in Fig. 2d) and 2D surface source (based on profiles in Fig. 2a) and compared their intensity profiles on the image plane in Fig. 2c. Because of the similar image intensity profiles in Fig. 2c, the relatively small three-dimensional fluorescence area can be approximated as a surface light source with the profile depicted in Fig. 2a for higher computational efficiency in simulations. Based on this, we obtained the physical dimensions and radiation profile of the fluorescence for subsequent simulation.

B. Simulation and Focal Power Division

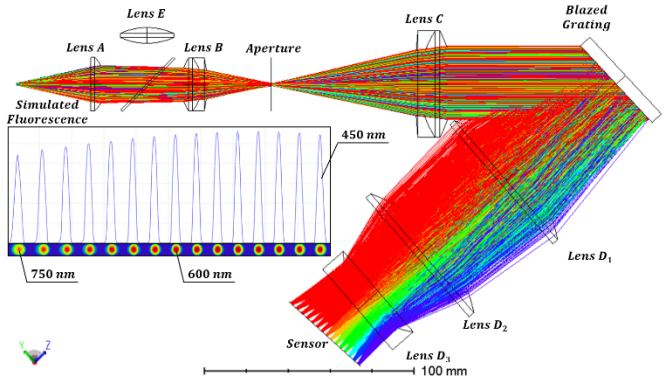

Fig. 3. ZEMAX simulation of the fluorescence sensor and radiance distribution on sensor plane for simulated wavelengths from 450 nm to 750 nm.

Fig. 3 shows a simulation of the fluorescence sensor along with the energy distribution on the sensor plane. It should be noted that aspheric lenses, despite their ability to eliminate spherical aberration and produce superior collimation, are more expensive and have fewer options or longer lead times. Therefore, in the simulation and system constructions, spherical optics were employed. Lens A, an uncoated UV fused-silica lens, was chosen for its superior transmission of both UV and

VIS wavelengths. To minimize chromatic aberration, lenses B and C were utilized as one and two-inch (respectively) anti-reflective (AR) coated achromatic doublets (400-700 nm). Seidel aberration theory posits that a positive lens typically creates a negative Petzval field curvature [27,28] and it is possible to correct this field curvature by dividing the power into multiple lens elements or incorporating a negative lens as a field flattener close to the image plane [29]. Accordingly, we divided the focal power into lenses D_1 and D_2 instead of employing a single lens. A negative lens, D_3, was also included close to the image plane to decrease the image field curvature. Introducing more lenses instead of a single lens also provides an additional advantage: the distances between lenses can be altered as variables in a subsequent optimization process.

C. Optimization

In selecting low-cost lenses from off-the-shelf optical components, lens parameters such as the radius of curvature are predetermined. Therefore, only the distances between lenses, and tilt angles of optic components are treated as variables for optimization. To prevent component overlap, boundaries for these variables are restricted using optimization operands FTGT (full thickness greater than) and FTLT (full thickness less than) for thickness boundaries, and PMGT (parameter greater than) and PMLT (parameter less than) for angular boundaries. For minimal spot size, optimization operands TRCX (transverse aberration in x direction) and TRCY (transverse aberration in y direction) are automatically generated in the merit function with the ZEMAX optimization wizards. Initially, a global search is conducted for minimal spot size, and subsequently, Hammer optimization is performed, utilizing DENC (diffraction encircled energy) operands for higher energy concentration. The post-grating effective focal length calculated by the EFL operand is 113.25 mm and the incident angle of the grating is 43.17°. Both values are closely aligned with our outcomes from nonlinear programming as detailed in section II.

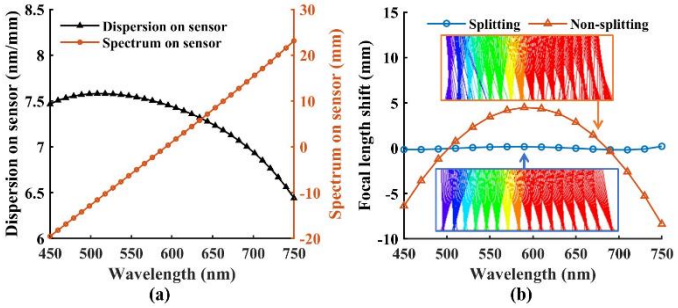

Fig. 4. (a) Simulated reciprocal linear dispersion and spectrum position on sensor plane. (b) Simulated image field curvature (focal length shifts for different wavelengths) when splitting or not splitting focal power.

Fig. 4a shows the simulated reciprocal linear dispersion, ranging from 6.4 to 7.6 nm/mm, which is in close proximity to our 7 nm/mm design target. The spectral distribution exhibited on the sensor plane maintains reasonable linearity. When focusing rays of the central wavelength (600 nm) onto the sensor plane, shorter and longer wavelength rays tend to focus in front of or behind the sensor plane, resulting in a curved image field. This shift in focal length can be utilized to represent the image field curvature. Fig. 4b depicts the image field curvature represented by focal length shift when focal power is either split or not split, using a single lens (LA1238, Thorlabs Inc., $110) or three lenses (LC1315, 2×LA1002, Thorlabs Inc., $262). Although splitting the focal power increases costs by approximately $150, the reduced surface curvature of the lenses results in decreased aberrations and a flatter image plane. As shown in Fig. 4b, the average focal length shift is significantly reduced from 3.47 mm to 0.12 mm.

D. Balancing Resolution and Sensitivity

When the NA values of Lenses A through E are established, the aperture size becomes the decisive factor for the quantity of light entering the spectrometer, as well as for the final spectral resolutions.

Spectral resolution, or spectral resolving power R, is a measure of the ability to resolve features in spectrum, and it is defined as [23]:

$$R = \frac{\lambda}{\Delta\lambda} \tag{6}$$

where $\Delta\lambda$ represents the minimum distinguishable difference in wavelengths at a given wavelength λ. A higher spectral resolution indicates a greater capability to resolve adjacent spectral peaks.

To discriminate between two adjacent peaks on the sensor, it is imperative that the separation between the peaks is adequate to produce an intensity valley depth ranging between 20% and 30% of the peak intensity [23,30]. In Fig. 5a, three distinct fluorescence spots with varying wavelengths that generate an intensity valley depth of roughly 25% of the peak intensity have been simulated.

The sensitivity of the system is characterized by the fluorescence collection efficiency, which is defined as the ratio of the energy received by the sensor to the available fluorescence energy within the system NA (0.3). As the aperture size increases from 0.8 to 1.2 mm, the collection efficiency experiences an upsurge from 17.8% to 39.3% as shown in Fig. 5a. Increasing the collection efficiency can lead to broader and higher spectral peaks, thereby reducing the ability to differentiate adjacent peaks due to increased overlap. So, the minimum spectral separation required to distinguish between adjacent peaks ($\Delta\lambda$) also increases from 5.75 to 8.25 nm as shown in Fig. 5a.

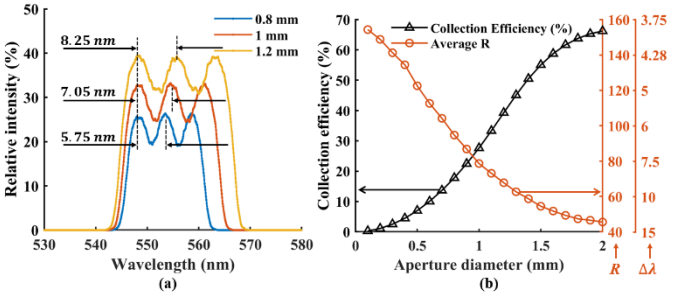

Fig. 5. (a) Simulated fluorescence intensity on the sensor plane given different aperture sizes. (b) Simulated fluorescence collection efficiency and average spectral resolution.

Fig. 5b depicts the simulated fluorescence collection efficiency trend and the average spectral resolution for different

aperture sizes. Notably, the collection efficiency shows a nearly hundred-fold increase from 0.2798% to 27.64% as the aperture size increases from 0.1 mm to 1 mm, due to the area-scaling of collection efficiency. However, as the aperture size grows, the average spectral resolution decreases while $\Delta\lambda$ increases from 3.8 nm to 13.1 nm. This implies that the spectral resolution deteriorates relatively slower than the increase in fluorescence signal with larger apertures. Additionally, the increase in fluorescence collection efficiency slows down gradually after the aperture size surpasses 1 mm. Considering these observations, we employed a 1 mm aperture in our experiments to strike a balance between spectral resolution and sensitivity.

IV. Experiments

A. Experiment Setup

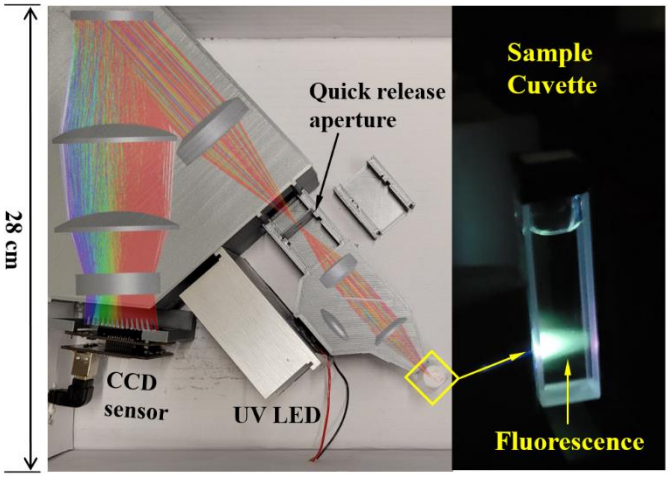

Fig. 6. Experiments setup fixed in a portable box.

As a proof-of-concept, the fluorescence sensor was deployed to detect economically critical emissive rare earth elements (REEs) in solution, an emerging application area for luminescent sensors [2,31-33]. REEs were selected as initial sensing targets for the fluorescence sensor due to their economic importance as well as their unique optical properties: unlike other metals, certain REEs are inherently emissive, and emit element-distinct emission bands [33,34]. Here, liquid samples of terbium (Tb), europium (Eu), samarium (Sm) and dysprosium (Dy), 4 visible-emitting REEs, were tested. All samples were dispersed in a bio-MOF solution [35], which is an anionic, porous, metal-organic framework and has been evaluated as a sensitizer material for low-ppm or even ppb-level REE detection following a previously reported experimental protocol [36].

Our sensor does not require critical alignment due to the large emitting area of the LED and the millimeter-level aperture size. The optical components were clamped between two 3D-printed holders from top and bottom, which were fixed inside a polylactic acid (PLA) plastic housing with wall thicknesses ranging from 2 mm to 3 mm. The 3D printer used was the Ultimaker 3 with a printing precision of 60 µm. ZEMAX simulations indicate that location errors of 60 µm have a negligible impact on the simulated spectrum obtained by the sensor. The entire structure is compact and portable, housed in a box with dimensions of 28 cm × 25 cm × 6 cm, as illustrated in Fig. 6. To ensure optimal transmission in the UV-VIS wavelength range, the sample cuvette (CV10Q35F, Thorlabs Inc.) is made of UV-fused Quartz glass. Quick-release slots are incorporated into the design, allowing for convenient changes in the aperture size to adjust for varying priorities of sensitivity and spectral resolution in future applications. Fluorescence signals were detected by a general-purpose CCD line sensor (TCD1304, Toshiba Inc.) featuring 3648 × 1 pixels and an integration time of 100 milliseconds. The total cost of our sensor is around 2000 USD.

B. Measurements and Results

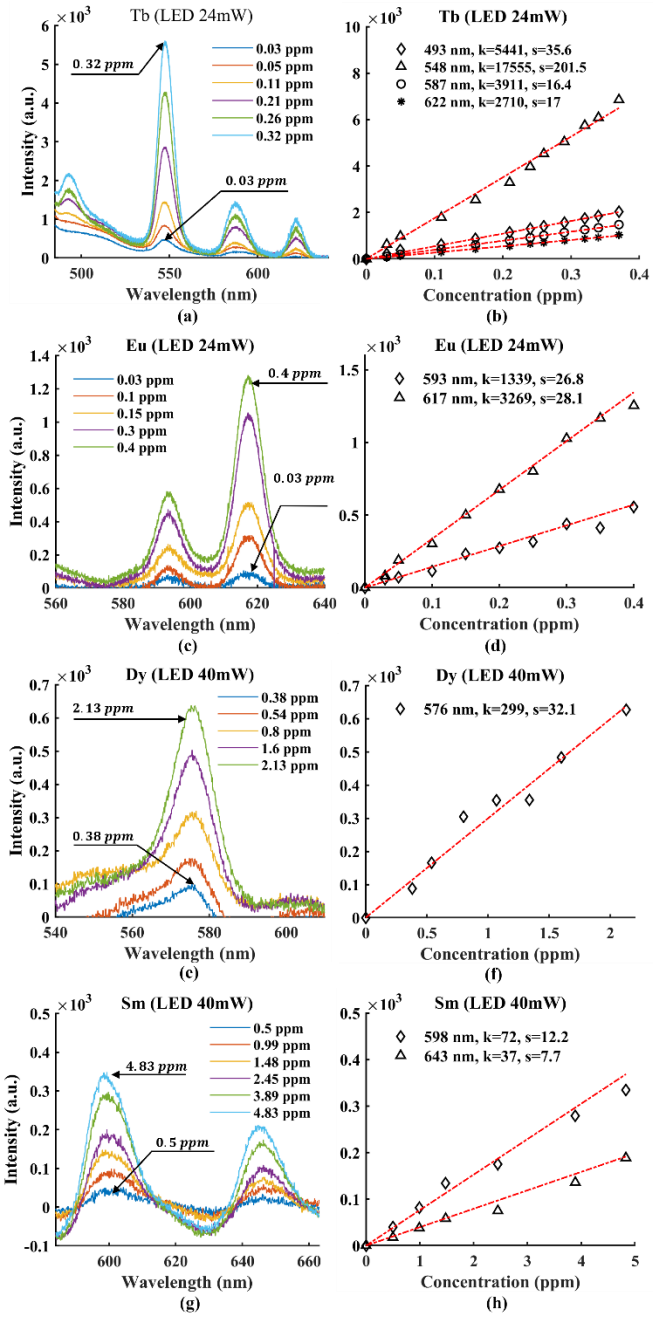

Fig. 7. Averaged fluorescence spectrum and linearly ($y=k*x$) fitted peak values for (a)(b) Tb at 24mW LED; (c)(d) Eu at 24mW LED; (e)(f) Dy at 40mW LED; (g)(h) Sm at 40mW LED.

Baseline measurements were initially conducted on

deionized water, followed by the addition of the MOF and subsequently, a small amount of a REE sample using a 10 µL titration pipette. The REE fluorescence signal was obtained by subtracting the MOF signal from the measured spectra. The spectra for each REE concentration level were measured at least seven times, and the average results for all four samples are presented in Fig. 7. To avoid over-exposure or exceeding the maximum intensity range of the CCD, the light source power was reduced to around 24mW (200mA DC current) for the stronger-emitting Tb and Eu samples, while the source power was increased to around 40mW (350mA DC current) for the weaker-emitting Dy and Sm samples. The CCD integration time was difficult to adjust dynamically due to circuit issues in this experiment. As a result, the power of the LED excitation source was reduced for samples with strong fluorescence emissions to avoid saturation in this experiment. However, it is worth noting that for blind testing, the excitation source power should remain stable and integration time should be adjusted to ensure proper dynamic sensing range. The output signal obtained with different integration times can be normalized using a linear relationship provided in the CCD datasheet.

The limits of detection (LOD) and limits of quantification (LOQ) of the system were determined based on the protocol laid out in Daniel Harris' *Quantitative Chemical Analysis* [37]. Linear fitting ($y=k*x$) was performed to find the slope (k) of the intensity vs. concentration of rare earth elements (REEs), as demonstrated in the right column of Fig. 7. The noise was estimated as the standard deviation (s) of at least 7 replicate measurements made after the first addition of Tb, Dy, Sm, and Eu. The LOD and LOQ were estimated as three and ten times of the signal-to-noise (k/s) ratio, respectively. A comparison of the LOD and LOQ of our fluorescence sensor with those of a commercial laboratory (HORIBA Jobin-Yvon Fluorolog 3 with FluorEssence software, a 450 W xenon arc lamp) was presented in Table 1, using the same sensing material, sensor integration time (100 millisecond) and experimental conditions previously reported in the literature [38]. Our fluorescence sensor demonstrated promising results in detecting rare earth elements (REE) at the parts per billion (ppb) level, even with reduced source power to prevent potential saturation of the CCD sensor when measuring samples with high concentrations of Tb and Eu. It is worth noting that the dynamic sensing range of the CCD sensor has a linear relationship with the integration time, as stated in its datasheet, and thus dynamic adjustment of the CCD integration time is recommended for future work.

TABLE I
COMPARISON OF LOD, LOQ AND SOURCE POWER

Sample	LOD (ppb)		LOQ (ppb)		Source power (Watt)	
	Our Sensor	Fluorolog 3	Our Sensor	Fluorolog 3	Our Sensor	Fluorolog 3
Tb	21 ± 3	**8 ± 1**	71 ± 10	**27 ± 4**	0.024	450
Eu	**43 ± 2**	70 ± 10	**143 ± 8**	220 ± 40	0.024	450
Dy	324 ± 26	**170 ± 10**	1081 ± 88	**550 ± 30**	0.04	450
Sm	**575 ± 42**	600 ± 90	**1917 ± 141**	2000 ± 300	0.04	450

In Fig. 7a, we can observe the presence of background signal at shorter wavelengths, notably at the 493 nm fluorescence peaks of Terbium. As a result, a linear fit of the form $y=kx+b$ was first performed, and the y-intercept b was subtracted from all peak values. The resulting peak values were then fitted using a linear function of the form $y=kx$, as shown in Fig. 7. This occurrence is likely attributed to the backscattering from the light source together with the stray light scattered by the polymer walls of the spectrometer. To address this issue, the inclusion of a long-pass filter following the dichroic mirror and further optical optimizations to mitigate stray light in the spectrometer are recommended in future work.

V. CONCLUSION

In this paper, we develop a low-cost optical system tailored for fluorescence optical emission with broad spectral features. Detection experiments with REE samples showed that the custom-spectrometer designed herein provides similar or slightly better sensitivities to a significantly more expensive desktop commercial instrumentation. Using inexpensive off-the-shelf optics and focal plane arrays, this paper shows that by balancing spectral resolution and sensitivity, it is possible to design low-cost, portable fluorescence sensors to achieve -ppb level of LOD while still harnessing sufficiently accurate spectral information for a wide array of applications. Taken together, this design and optimization approach should enable other researchers and designers to perform similar application-specific work.

VI. DISCLAIMER

This project was funded by the United States Department of Energy, National Energy Technology Laboratory, in part, through a site support contract. Neither the United States Government nor any agency thereof, nor any of their employees, nor the support contractor, nor any of their employees, makes any warranty, express or implied, or assumes any legal liability or responsibility for the accuracy, completeness, or usefulness of any information, apparatus, product, or process disclosed, or represents that its use would not infringe privately owned rights. Reference herein to any specific commercial product, process, or service by trade name, trademark, manufacturer, or otherwise does not necessarily constitute or imply its endorsement, recommendation, or favoring by the United States Government or any agency thereof. The views and opinions of authors expressed herein do not necessarily state or reflect those of the United States Government or any agency thereof.

REFERENCES

[1] Lakowicz, J. R., "Instrumentation for Fluorescence Spectroscopy, " in *Principles of Fluorescence Spectroscopy*, 3rd ed. New York, NY, USA: Springer, 2006, pp. 32-34.

[2] Crawford, Scott E., Paul R. Ohodnicki, and John P. Baltrus, "Materials for the photoluminescent sensing of rare earth elements: challenges and opportunities, " *Journal of Materials Chemistry C*, vol. 8, no. 24, pp. 7975-8006, 2020.

[3] Shin, Young-Ho, Jonathan Z. Barnett, M. Teresa Gutierrez-Wing, Kelly A. Rusch, and Jin-Woo Choi, "A hand-held fluorescent sensor platform for selectively estimating green algae and cyanobacteria biomass," Sensors and Actuators B: Chemical, no. 262, pp. 938-946, 2018.

[4] Cotruvo Jr, Joseph A., Allegra T. Aron, Karla M. Ramos-Torres, and Christopher J. Chang, "Synthetic fluorescent probes for studying copper

in biological systems," Chemical Society Reviews 44, no. 13, pp. 4400-4414, 2015.
[5] Aron, Allegra T., Karla M. Ramos-Torres, Joseph A. Cotruvo Jr, and Christopher J. Chang, "Recognition-and reactivity-based fluorescent probes for studying transition metal signaling in living systems," Accounts of chemical research 48, no. 8, pp. 2434-2442, 2015.
[6] Zhang, Qi, Chen-Feng Wang, and Yun-Kai Lv., "Luminescent switch sensors for the detection of biomolecules based on metal–organic frameworks," *Analyst*, vol. 143, no. 18, pp. 4221-4229, 2018.
[7] Kong, Fanning, et al., "A novel fluorescent probe of alkyne compounds for putrescine detection based on click reaction," *RSC advances*, vol. 12, no. 41, pp. 26630-26638, 2022.
[8] Borecki, Michal, Mateusz Geca, and Michael L. Korwin-Pawlowski, "Automotive Diesel Fuel Internal Stability Testing with the Use of UV and Temperature as Degradation Factors," *Materials*, vol. 15, no. 23, pp. 8548, 2022.
[9] Shin, Young-Ho, Jonathan Z. Barnett, Edward Song, M. Teresa Gutierrez-Wing, Kelly A. Rusch, and Jin-Woo Choi, "A portable fluorescent sensor for on-site detection of microalgae," Microelectronic Engineering, no. 144, pp. 6-11, 2015.
[10] Shin, Young-Ho, M. Teresa Gutierrez-Wing, and Jin-Woo Choi, "A field-deployable and handheld fluorometer for environmental water quality monitoring," Micro and Nano Systems Letters 6, no. 1, pp. 1-6, 2018.
[11] Zieger, Silvia E., Günter Mistlberger, Lukas Troi, Alexander Lang, Fabio Confalonieri, and Ingo Klimant, "Compact and low-cost fluorescence-based flow-through analyzer for early-stage classification of potentially toxic algae and in situ semiquantification," Environmental science & technology 52, no. 13, pp. 7399-7408, 2018.
[12] Tahirbegi, Islam Bogachan, Josef Ehgartner, Philipp Sulzer, Silvia Zieger, Alice Kasjanow, Mirco Paradiso, Martin Strobl, Dominique Bouwes, and Torsten Mayr, "Fast pesticide detection inside microfluidic device with integrated optical pH, oxygen sensors and algal fluorescence," Biosensors and Bioelectronics no. 88, pp. 188-195, 2017.
[13] De Acha, Nerea, César Elosúa, Jesús M. Corres, and Francisco J. Arregui, "Fluorescent sensors for the detection of heavy metal ions in aqueous media," Sensors 19, no. 3, pp. 599, 2019.
[14] Crawford, Scott E., Michael J. Hartmann, and Jill E. Millstone., "Surface chemistry-mediated near-infrared emission of small coinage metal nanoparticles," *Accounts of Chemical Research*, vol. 52, no. 3, pp. 695-703, 2019.
[15] Owen, Jonathan, and Louis Brus., "Chemical synthesis and luminescence applications of colloidal semiconductor quantum dots," *Journal of the American Chemical Society*, vol 139, no. 32, pp. 10939-10943, 2017.
[16] Bekenstein, Yehonadav, *et al*., "Highly luminescent colloidal nanoplates of perovskite cesium lead halide and their oriented assemblies," *Journal of the American Chemical Society*, vol. 137, no. 51, pp. 16008-16011, 2015.
[17] Schmidt, Oliver, Peter Kiesel, and Michael Bassler, "Performance of chip-size wavelength detectors," *Optics Express*, vol. 15, no. 15, pp. 9701-9706, 2007.
[18] Medintz, Igor L., *et al*., "Resonance energy transfer between luminescent quantum dots and diverse fluorescent protein acceptors," *The Journal of Physical Chemistry C*, vol. 113, no. 43, pp. 18552-18561, 2009.
[19] Crawford, Scott E., *et al*., "Efficient energy transfer from near-infrared emitting gold nanoparticles to pendant Ytterbium (III)," *Journal of the American Chemical Society*, vol. 139, no. 49, pp. 17767-17770, 2017.
[20] Shang, Xin, et al., "Fluorogenic protein labeling using a genetically encoded unstrained alkene," Chemical science, vol. 8, no. 2, pp. 1141-1145, 2017.
[21] Shin, Young-Ho, M. Teresa Gutierrez-Wing, and Jin-Woo Choi, "Recent progress in portable fluorescence sensors," Journal of The Electrochemical Society, vol. 168, no. 1, pp. 017502, 2021.
[22] Semrock, Inc., "Semrock Master Catalog," FF347-Di01 datasheet, pp. 62, 2019.
[23] Palmer, C., *Diffraction grating handbook*, 8th ed., MKS instruments, Inc., New York, NY, USA, 2005, pp. 21-29.
[24] MATLAB version 9.10.0.1649659 (R2021a), The MathWorks, Inc., Natick, MA, United States.
[25] Greivenkamp, John E., *Field guide to geometrical optics*, Vol. 1., SPIE press, Bellingham, Washington, 2004, pp. 29.
[26] Luminus Devices, Inc., "XST-3535-UV Surface Mount UVC LED," XST-3535-UV datasheet, 2020, pp. 2-6.
[27] Gross, Herbert, ed., *Handbook of Optical Systems, Volume 3: Aberration Theory and Correction of Optical Systems*, 1st ed., Vol. 3. Wiley-Vch, 2005.
[28] Nie, Yunfeng, *et al*., "Optical design of freeform mirror systems with tailored field curvatures for corneal imaging," In *International Optical Design Conference*. Optical Society of America, Denver, Colorado, Jul. 9-13, 2017, pp. JW2C-1.
[29] Kwon, Jong-Hoon, *et al*., "Field-curvature correction according to the curvature of a CMOS image-sensor using air-gap optimization," *Journal of the Optical Society of Korea*, vol. 19, no. 6, pp. 658-664, 2015.
[30] Ball, David Warren., *The basics of spectroscopy*. Vol. 49., SPIE press, Bellingham, Washington, 2001, pp. 105-108.
[31] Mattocks, Joseph A., Jackson V. Ho, and Joseph A. Cotruvo Jr, "A selective, protein-based fluorescent sensor with picomolar affinity for rare earth elements," Journal of the American Chemical Society 141, no. 7, pp. 2857-2861, 2019.
[32] Essawy, Amr A, "Highly selective antenna effect in polystyrene membrane immobilized 2-pyridone sensitizer: Novel spectrofluorimetric method for assessment of nano scale terbium (III)," Sensors and Actuators B: Chemical, no. 196, pp. 640-646, 2014.
[33] Attia, M. S., Amr A. Essawy, and A. O. Youssef, "Europium-sensitized and simultaneous pH-assisted spectrofluorimetric assessment of ciprofloxacin, norfloxacin and gatifloxacin in pharmaceutical and serum samples," Journal of Photochemistry and Photobiology A: Chemistry, no. 236, pp. 26-34, 2012.
[34] Bünzli, Jean-Claude G., and Claude Piguet., "Taking advantage of luminescent lanthanide ions," *Chemical Society Reviews*, vol. 34, no. 12, pp. 1048-1077, 2005.
[35] An, Jihyun, *et al*., "Synthesis and characterization of a new anionic zinc-adeninate metal-organic framework [Zn3 (ad)(BTC) 2·(Me2NH2), 5.75 DMF, 0.25 H2O]," *Journal of Porous Materials*, vol. 22, no. 4, pp. 867-875, 2015.
[36] Crawford, Scott E., *et al*., "Zinc-Adeninate metal–organic framework: A versatile Photoluminescent sensor for rare earth elements in aqueous systems," *ACS sensors*, vol. 4, no. 8, pp. 1986-1991, 2019.
[37] Harris, Daniel C., *Quantitative chemical analysis*, 10th ed., Macmillan, 2010, pp 104-105.
[38] Crawford, Scott E., *et al*., "Influence of the anionic zinc-adeninate metal–organic framework structure on the luminescent detection of rare earth ions in aqueous streams," *ACS Applied Materials & Interfaces*, vol. 13, no. 6, pp. 7268-7277, 2021.